NANO LETTERS
Letter
Cite This: Nano Lett. XXXX, XXX, XXX−XXX
pubs.acs.org/NanoLett

Stable and Highly Ion-Selective Membrane Made from Cellulose Nanocrystals for Aqueous Redox Flow Batteries

Alolika Mukhopadhyay,[†] Zheng Cheng,[†] Avi Natan,[†] Yi Ma,[‡] Yang Yang,[†] Daxian Cao,[†] Wei Wang,*[,‡] and Hongli Zhu*[,†]

[†]Department of Mechanical and Industrial Engineering, Northeastern University, 360 Huntington Avenue, Boston, Massachusetts 02115, United States

[‡]Rogers Corporation Innovation Center, 141 South Bedford Street, Burlington, Massachusetts 01803, United States

Supporting Information

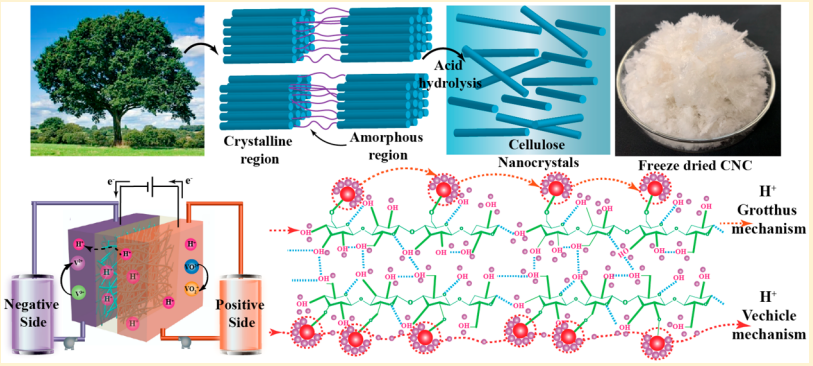

ABSTRACT: The design of chemically stable ion-exchange membranes with high selectivity for applications in an aqueous redox flow battery (RFB) at high acid concentrations remains a significant challenge. Herein, this study designed a stable and highly ion-selective membrane by utilizing proton conductive cellulose nanocrystals (CNCs) incorporated in a semicrystalline hydrophobic poly(vinylidene fluoride-*co*-hexafluoropropylene) (PVDF-HFP) matrix. The high hydrophobicity of the PVDF-HFP matrix mitigates crossover of the electrolytes, whereas the abundant and low-cost CNCs derived from wood provide high proton conductivity. The fundamental contributors for CNCs' excellent proton conductivity are the hydroxyl (−OH) functional groups, highly acidic sulfonate ($-SO_3H$) functional groups, and the extensive intramolecular hydrogen bonding network. In addition, CNCs exhibit a mechanically and chemically stable structure in the harsh acidic electrolyte attributed to the high crystallinity (crystalline index of ∼86%). Therefore, because of the high proton conductivity, excellent ion selectivity, high chemical stability, and structural robustness, the vanadium redox flow battery (VRFB) assembled with the homogeneous CNCs and PVDF-HFP (CNC/PVDF-HFP) membrane achieved a Coulombic efficiency (CE) of 98.2%, energy efficiency (EE) of 88.2%, and a stable cycling performance for more than 650 cycles at a current density of 100 mA cm^{-2}. The obtained membrane possesses excellent flexibility, high mechanical tensile strength, and superior selectivity. Meanwhile, the applied casting method is scalable for large-scale manufacturing.

KEYWORDS: *Ion-exchange membrane, redox flow battery, cellulose nanocrystal, proton conductivity, vanadium, hydrogen bonding*

Over the past few years, redox flow batteries (RFBs) have gained immense attention and are now regarded as the ideal choice for large-scale energy storage due to numerous attractive features such as excellent electrochemical reversibility, long life, high Coulombic efficiency, and decoupling of energy and power storage capability. Regardless of the compelling merits, wide-scale commercial utilization of RFBs has been burdened by the high cost and low selectivity of the commonly used perfluorinated membrane, known as Nafion.[1] The current membrane accounts for ∼17% of the total cost of flow batteries.[2] Ion-exchange membranes in the flow battery act as a physical barrier to separate the positive and negative half-cells and simultaneously allow migration of charge-balancing ions from one side to the other to complete the internal circuit of the cell.[3] The RFB's overall performance heavily depends on the properties of the ion-exchange membranes (IEMs). To reduce energy loss, it is essential for the IEMs to have high ionic conductivity while preventing crossover of active species to ensure low area-specific resistance (ASR) and high Coulombic efficiency.[4] Therefore, significant efforts have been devoted in search for scalable and high-performance membranes possessing high chemical stability, high selectivity, and excellent proton conductivity especially under a strongly acidic environment.

Received: September 25, 2019
Revised: November 6, 2019
Published: November 8, 2019

DOI: 10.1021/acs.nanolett.9b03964
Nano Lett. XXXX, XXX, XXX−XXX

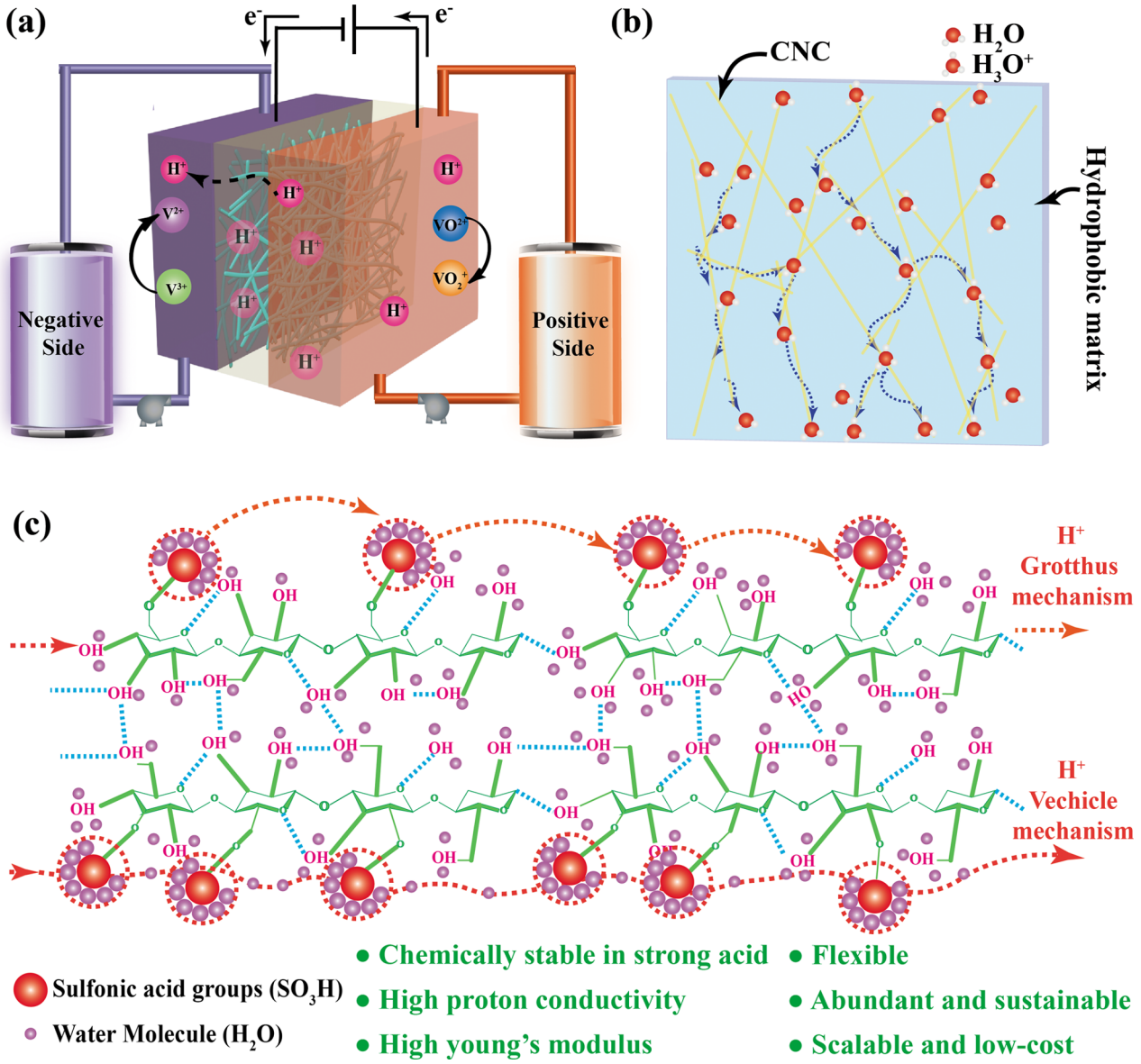

Figure 1. Schematic illustration of (a) a flow cell utilizing the CNC/PVDF-HFP membrane, (b) two-phase structure of the CNC/PVDF-HFP membrane, and (c) proton conduction mechanism of the CNC/PVDF-HFP membrane.

Traditionally, state-of-the-art Nafion membranes are predominantly used in RFB because of their excellent stability and high ionic conductivity. Nevertheless, severe migration of vanadium ions affects the overall performance, and high cost limits the extensive application of the Nafion in RFB. To improve the selectivity of the Nafion membranes, several organic and inorganic fillers such as SiO_2,[5] TiO_2,[6] amino silica nanoparticles,[7] zeolites,[8] polyelectrolytes,[9] polyanilines,[10] polypyrroles,[11] sulfonated polyether ketone (SPEEK),[12] and more have been incorporated into the Nafion membranes. However, the cost of Nafion-based membranes remains a challenge. Sulfonated or quaternized nonperfluorinated membranes were also investigated due to their advantageous combination of tunable ionic conductivity, high selectivity, and low cost. However, they hardly satisfy the required criteria for large-scale and long-lasting RFBs due to their poor chemical stability arising from the presence of the ion-exchange groups.[13] Therefore, there is an urgent need to develop low-cost membranes with tunable ionic conductivity, high selectivity, and excellent mechanical and chemical stability.

Cellulose nanocrystals (CNCs), a renewable, biodegradable, and sustainable nanomaterial, are derived from abundant resources, such as wood with strong acid hydrolysis, and have considerable potential as a building block for super strong materials.[14] While wood pulp is a potential main source of CNCs, it is possible to produce CNCs from diverse starting materials such as: algae, bacteria, bast fibers, cotton linters, and tunicin.[15] They are prepared in strong sulfuric acid (60−64 wt % concentration); therefore, the obtained CNCs have superior stability in acidic conditions. Meanwhile, the primary unit of the cellulose molecule is glucose, which has six hydroxyl groups in each repeat unit. Due to the enormous amount of hydroxyl groups, the CNCs are extremely hydrophilic. CNC is an abundant resource with an annual production rate of 13870t at a manufacturing cost of ~3.6−4.4 $/kg manufacturing cost.[16,17] CNCs have attracted broad attention and are considered as one of the ideal reinforcing fillers due to their

DOI: 10.1021/acs.nanolett.9b03964
Nano Lett. XXXX, XXX, XXX−XXX

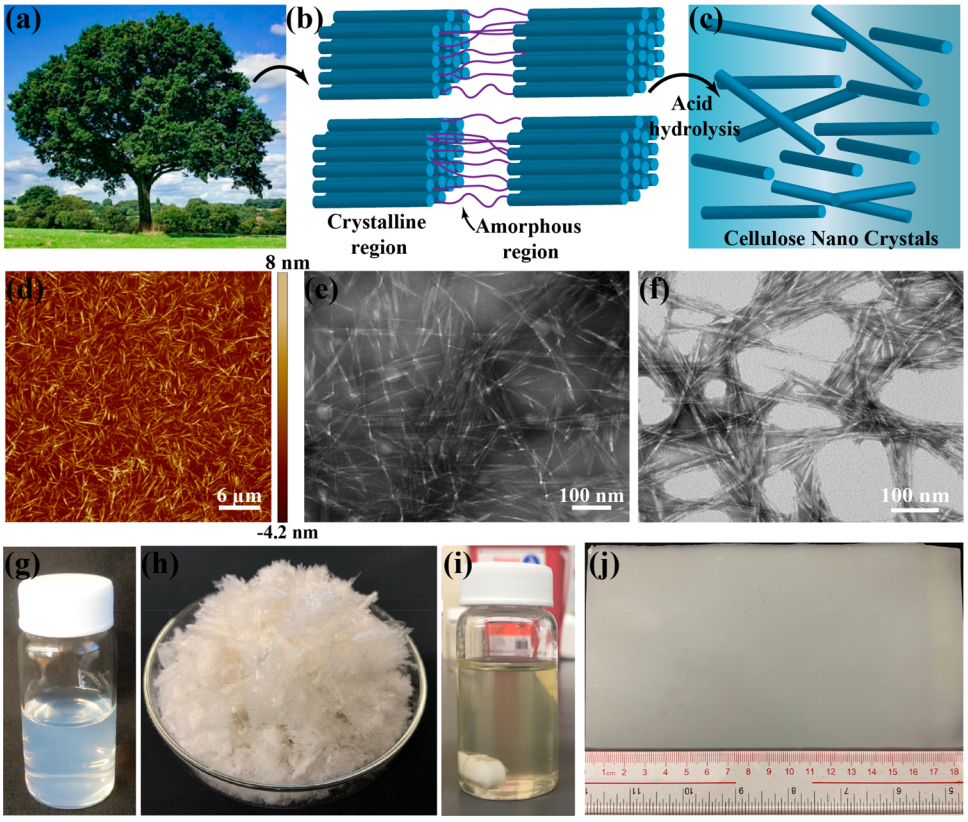

Figure 2. (a) Trees from where cellulose is obtained. Schematic illustration of (b) cellulose microfibrils containing crystalline and amorphous regions and (c) cellulose nanocrystals obtained from sulfuric acid hydrolysis of cellulose microfibrils. (d) AFM image of CNCs. (e) A TEM image of dried dispersion of CNCs highlighting the submicron size and high aspect ratio of CNCs. (f) A high magnification TEM image of CNCs, showing the interconnectivity between the CNC's nanorods. Digital photographs of (g) CNCs dispersed in an aqueous solution, (h) Freeze-dried CNCs, (i) homogeneous CNC/PVDF-HFP mixture in DMF, and (j) CNC/PVDF-HFP composite membrane prepared by solution casting of the CNC/PVDF-HFP blend and then calendaring.

appealing intrinsic properties such as nanoscale dimensions (3−20 nm wide, 50−2000 nm long), high aspect ratio (10−30), low density (~1.6 g cm^{-3}), high tensile strength (~7 GPa) and Young's modulus (~150 GPa), low coefficient of thermal expansions (~1 ppm/K), and thermal stability up to ~300 °C.[18−21] Previously, CNCs have been incorporated into a wide range of polymer matrices such as resin[22,23] as a mechanical strength enhancer. However, it is incredibly challenging to obtain well-dispersed hydrophilic CNCs in the hydrophobic polymer matrix using an organic solvent due to solvent incompatibility.

Herein, a new type of proton conductive membrane for RFB is made of highly hydrophobic PVDF-HFP and super-hydrophilic CNCs by freeze-drying the CNCs to eliminate incompatibilities with organic solvents and obtain a homogeneous dispersion of CNCs in the PVDF-HFP matrix. Both the PVDF-HFP and CNCs are stable in the strong oxidative environment of acidic RFBs due to the high crystallinity of both the polymers. Besides, PVDF-HFP also possesses high chemical and thermal resistance due to the fluorine-containing backbone. In the two-phase composite membrane, CNCs provide high proton conductivity to the membrane due to their excellent hydrophilicity, whereas, the PVDF-HFP hydrophobic skeleton offers the membrane selectivity to ensure successful RFB operation. Remarkably, the cost of the composite membrane is significantly lower than Nafion, because of the low cost of the starting materials and the vast abundance of the natural biopolymer cellulose. More importantly, the membrane demonstrated a superior cycling performance for more than 650 stable cycles at a current density of 100 mA cm^{-2} with an average CE of 98.2%, VE of 89.9%, and EE of 88.2% in the RFB. Therefore, the approach of constructing a low-cost and highly stable membrane holds great promise to significantly reduce the cost of the RFB stack and promotes the possibility of large-scale commercialization of RFB as an effective and low-cost energy storage technology.

Results and Discussion. The performance of the proposed CNC/PVDF-HFP proton conductive membrane was evaluated in a vanadium redox flow battery (Figure 1a), where ion transport properties are the key factors in defining the batteries' performance. The proton-conductive CNC/PVDF-HFP membrane is composed of CNCs incorporated in a hydrophobic PVDF-HFP matrix. The robust two-phase microstructure (Figure 1b) is beneficial because the hydrophilic region promotes proton conductivity, while the hydrophobic region prevents the cross-mixing of electrolytes. The protons in the CNC/PVDF-HFP membrane are predominantly transported by a combination of Grotthuss and vehicle mechanism, as shown in Figure 1c. The proton transportation through the Grotthuss mechanism occurs by hopping of proton from a donor to the nearest proton acceptor within the hydrogen bond network, which depends on the interconnectivity of the ionic clusters in the membrane.[24] In the CNC/PVDF-HFP membrane, CNCs contain plenty of hydroxyl (−OH) groups, and part of these surface −OH groups are converted to highly acidic sulfonate ($-SO_3H$)

DOI: 10.1021/acs.nanolett.9b03964
Nano Lett. XXXX, XXX, XXX−XXX

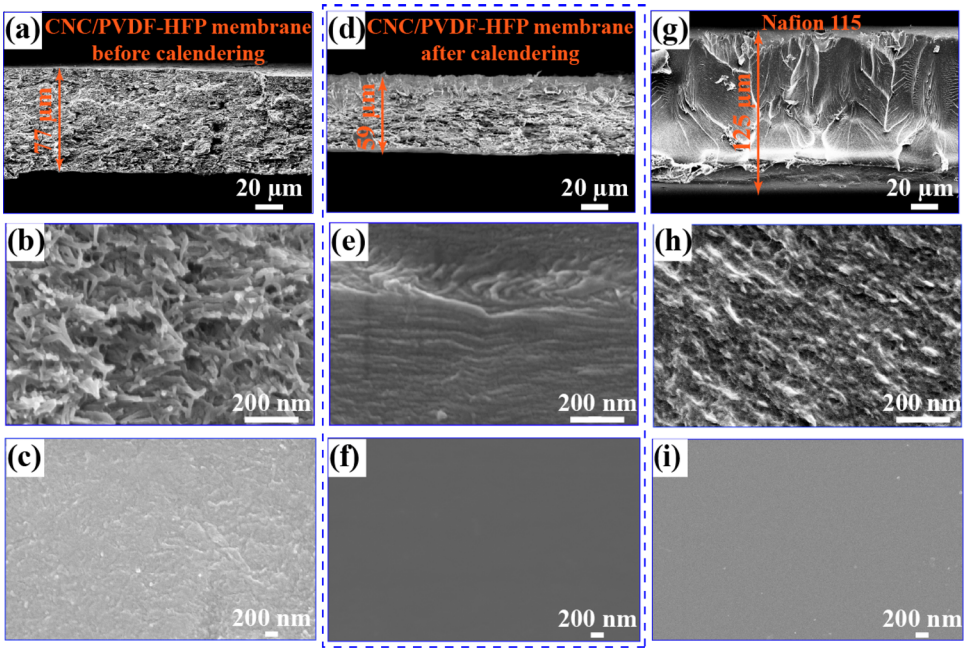

Figure 3. SEM images of (a, b) the cross section of the CNC/PVDF-HFP composite membrane before calendering at different magnifications, (c) The surface morphology of the CNC/PVDF-HFP composite membrane before calendering, (d, e) the cross section of CNC/PVDF-HFP composite membrane after calendering at different magnifications, (f) surface morphology of the CNC/PVDF-HFP composite membrane after calendering, (g, h) the cross section of the Nafion 115 membrane at different magnifications, and (i) surface morphology of the Nafion 115 membrane.

groups during the sulfuric acid hydrolysis of the cellulose fibers.[25] These inherent ion-exchange groups (−OH and $-SO_3H$) of CNCs assist in proton conduction through the Grotthuss mechanism by forming highly interconnected ionic nanoclusters. In addition, CNCs exhibit extensive intramolecular hydrogen-bond networks, extending from the hydroxyl of one unit to the oxygen of another unit,[14] which ensures continuous proton transfer channels in the membrane, yielding high proton conductivity via the Grotthuss mechanism. Contrarily, the vehicle mechanism involves proton diffusion with the carrier to transport acidic media solvated ions[26,27] and depends on the concentrations of the ions present in the system. The presence of sufficient hydroxyl groups in the CNC/PVDF-HFP membrane increases the water absorption by the membrane, leading to a better pathway for proton transfer through the vehicle mechanism. Therefore, the existence of abundant ion-exchange groups, the interconnectivity of the ionic nanoclusters due to the extensive hydrogen bonding, and acidity of the ion-conducting groups in the CNC/PVDF-HFP membrane enhance the proton conductivity. Besides, the material cost of the membrane was also calculated (Table S1), which is much lower than that of the commercial Nafion 115 membrane. Most importantly, CNCs meet all criteria of attaining high proton conductivity, and therefore, the CNC/PVDF-HFP membrane can be considered as an ideal and low-cost alternative to the Nafion membrane.

The CNCs are unique nanomaterials derived from naturally occurring bulk cellulose fibers extracted from trees (Figure 2a). The bulk cellulose contains highly ordered crystalline regions along with some disordered, amorphous regions (Figure 2b). The primary process for the isolation of CNCs from cellulose fibers is through acid hydrolysis, which preferentially hydrolyzes the disordered and paracrystalline regions (Figure 2c); however, the crystalline regions remain intact because of their high resistance to the acid attack.[14] The as-prepared CNC has a crystalline index of ~86% (eq 1 and Figure S1). Sulfuric acid reacts with the surface hydroxyl groups of the cellulose to yield surface sulfonate groups. Furthermore, to investigate the morphology of CNCs, atomic force microscopy (AFM) and transmission electron microscopy (TEM) were analyzed. Figure 2d displays the height mode image of CNCs, highlighting the morphology and size distribution. The TEM images of CNCs at different magnifications (Figure 2e,f) demonstrate a rod-like morphology of CNCs (3−5 nm in width and 100−200 nm in length), which verifies the high aspect ratio of the CNCs. This high aspect ratio of CNCs is exceptionally beneficial for forming interconnected hydrophilic nanochannels that promote the proton conduction through the membrane.

Furthermore, The CNCs are made up of linear cellulose chains (Figure S2), which are composed of glucose molecules with two anhydroglucose rings ($C_6H_{10}O_5$) in one repeat unit. Therefore, CNCs can be dispersed in water extremely well (Figure 2g) due to their intrinsic high hydrophilicity. However, due to their hydrophilicity, CNCs must have all of their water removed in order to blend them with PVDF-HFP, so the aqueous dispersion of CNCs was freeze-dried (Figure 2h) to form solid CNCs and dispersed in dimethylformamide (DMF). Currently, there are several applications of CNC require dried CNC, and most conventional methods for drying CNC are air drying, spray drying, supercritical drying, and freeze-drying.[28,29] However, different drying methods will result in CNC with a different thermal stability and crystallinity index. According to Peng et al., air-dried CNC provided a lower surface area compared to the other methods. In addition, Peng et al. reported that the CNC dried using supercritical-drying has the lowest thermal stability and crystallinity index, whereas the freeze-dried CNC has the highest thermal stability

DOI: 10.1021/acs.nanolett.9b03964
Nano Lett. XXXX, XXX, XXX−XXX

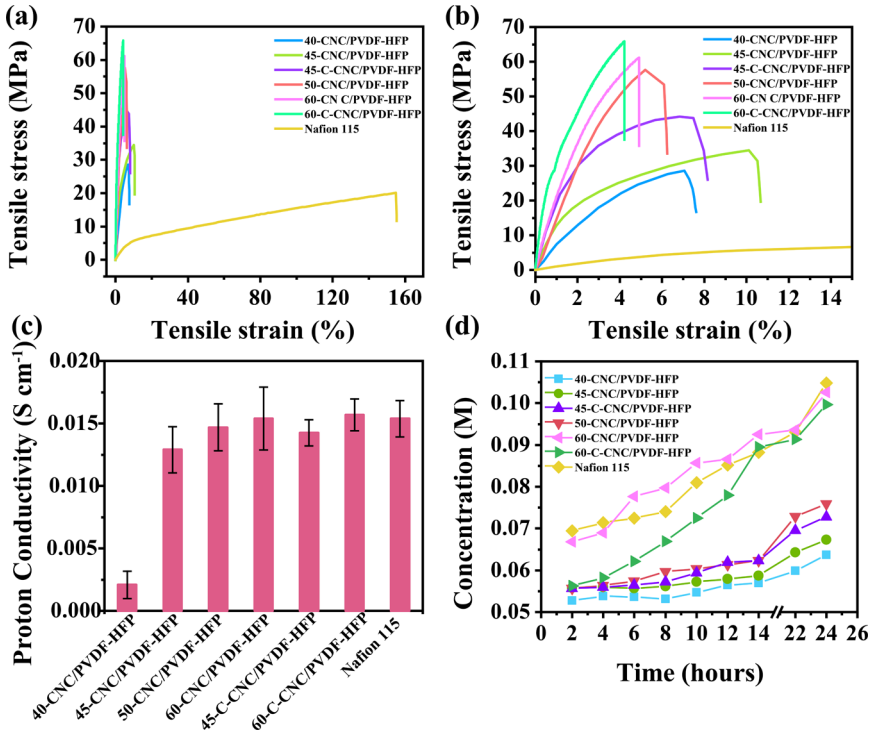

Figure 4. (a) Full range stress vs strain curves and (b) zoomed-in stress vs strain curves for 40-CNC/PVDF-HFP, 45-CNC/PVDF-HFP, 50-CNC/PVDF-HFP, 60-CNC/PVDF-HFP, 45-C−CNC/PVDF-HFP, 60-C−CNC/PVDF-HFP, and Nafion 115 membranes. (c) Proton conductivity of 40-CNC/PVDF-HFP, 45-CNC/PVDF-HFP, 50-CNC/PVDF-HFP, 60-CNC/PVDF-HFP, 45-C−CNC/PVDF-HFP, 60-C−CNC/PVDF-HFP, and Nafion 115 membranes. (d) Vanadium ion (VO^{2+}) permeability of 40-CNC/PVDF-HFP, 45-CNC/PVDF-HFP, 50-CNC/PVDF-HFP, 60-CNC/PVDF-HFP, 45-C−CNC/PVDF-HFP, 60-C−CNC/PVDF-HFP, and Nafion 115 membranes over 24 h.

among the others.[29] We have also investigated the morphology of the freeze-dried CNC powder and its dispersion in water and DMF using their SEM morphologies. The SEM image of freeze-dried CNC is presented in Figure S3a, from which we can see the CNC appears in an agglomerated form after freeze-drying. However, the freeze-dried CNC can be redispersed uniformly in both water and DMF, as shown in Figure S3b−f. The SEM images of redispersed CNC in water (Figure S3c,d) exhibit a particle size less than 50 nm. However, the particle size is not very clear in the SEM images of redispersed CNC in DMF (Figure S3e,f). Therefore, a dynamic light scattering measurements were also conducted (Figure S4), which indicated an average particle size of ∼156 nm in water and ∼196 nm in DMF. The obtained results verify the dispersibility of freeze-dried CNC in water and DMF, which is extremely crucial for the uniformity of the membrane.

Furthermore, the dispersion of CNCs in DMF was mixed with a 10 wt % PVDF-HFP solution in DMF to obtain varying weight percentages of CNCs (ranging from 40−60%) to prepare the slurry for casting. The shear blended CNC/PVDF-HFP slurry (Figure 2i) was cast using an automatic casting coater to obtain a uniform membrane of controlled thickness. After solvent evaporation, the membranes were tested as it is and also calendared into a homogeneous flat sheet. To illustrate the membrane's scalability, it was prepared at a larger scale, as shown in Figure 2j. The membrane exhibits a homogeneous surface without any visible defects and contains nanopores of ∼10 Å (Figure S5).

Moreover, the scanning electron microscope (SEM) images of the cross section and surface of the CNC/PVDF-HFP composite membrane before and after calendaring were used to investigate the morphology of the as-prepared membrane. Before calendaring, the cross-sectional images (Figure 3a,b) of the membrane display a uniform and homogeneous morphology, but the appearance of micro and nanovoids is apparent, and the surface morphology appears to be coarse (Figure 3c). Conversely, the calendared CNC/PVDF-HFP composite membrane appears to be denser and more uniform with no visible voids even at higher magnifications, as depicted in the cross-sectional images (Figure 3d,e) and surface (Figure 3f) morphology. Figure 3g,h exhibit the cross-sectional morphologies of Nafion 115 at different magnifications, and Figure 3i represents the surface profile of Nafion 115. No visible differences in the morphologies of the CNC/PVDF-HFP composite membrane after calendaring and Nafion 115 were observed. Therefore, it is evident that the calendaring process aids in eliminating the micro and nanovoids, making the membrane more uniform and dense, which achieves higher ionic selectivity by preventing the vanadium crossover through the defects.

In addition to the visible properties of the membrane, mechanical properties of the membranes are of significant concern for the long-term stability and performance of an RFB. To investigate if the mechanical properties of the CNC/PVDF-HFP membranes are satisfactory for implementing in an RFB, typical tensile stress−strain curves were evaluated. The different weight percent containing CNC samples are designated as X-CNC/PVDF-HFP, where X represents the weight percent of CNCs in the membrane, whereas the calendered membranes were designated as X-C−CNC/PVDF-HFP, where X represents the weight percent of CNCs in the membrane. Figure 4a,b exhibits the stress−strain curves for 40-CNC/PVDF-HFP, 45-CNC/PVDF-HFP, 50-CNC/PVDF-HFP, 60-CNC/PVDF-HFP, 45-C−CNC/PVDF-HFP 60-C−

DOI: 10.1021/acs.nanolett.9b03964
Nano Lett. XXXX, XXX, XXX−XXX

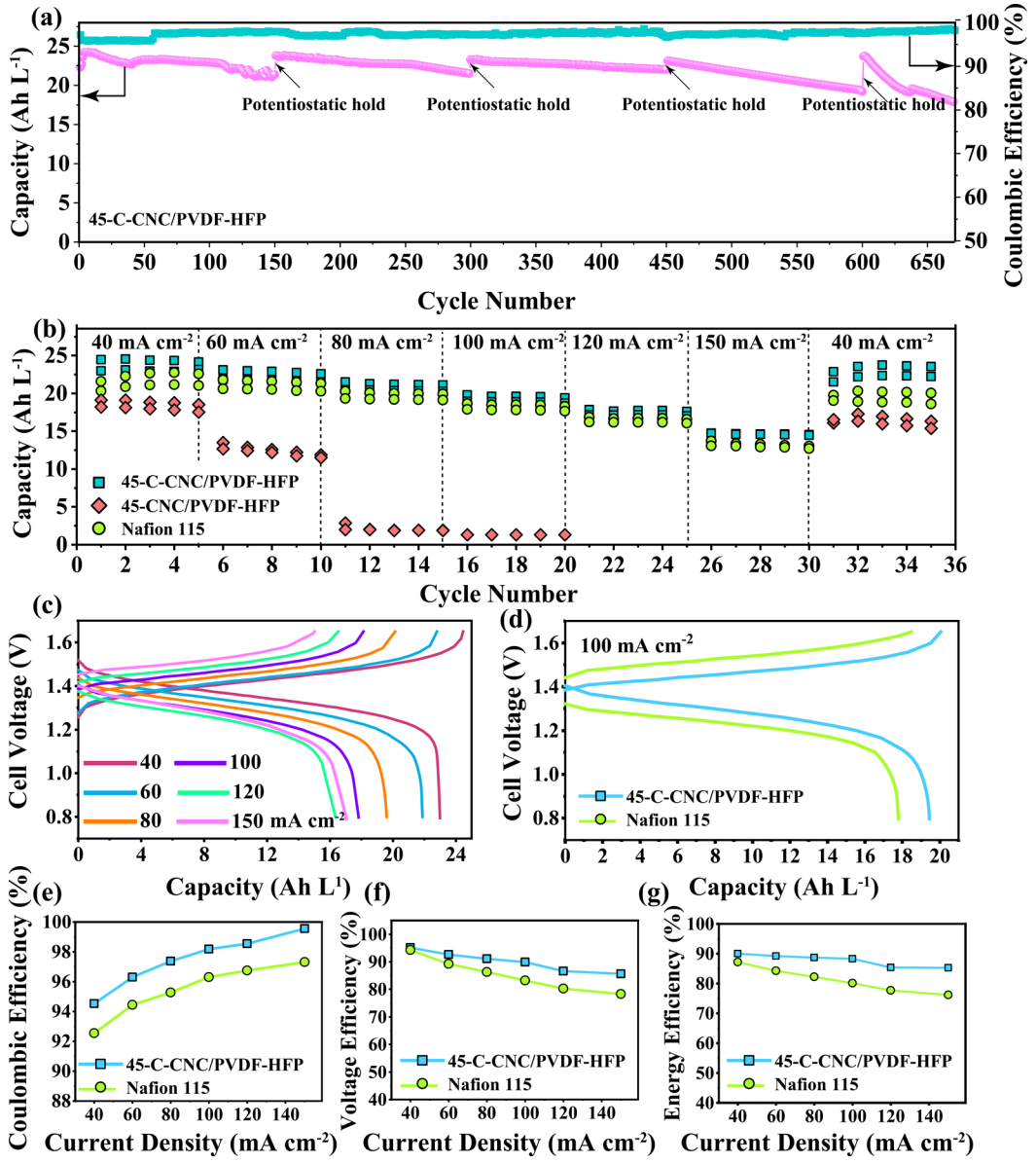

Figure 5. Performance of VRFB assembled using 45-C−CNC/PVDF-HFP and commercial Nafion 115 membranes. (a) Cycling stability representing the discharge capacity and CE of 45-C−CNC/PVDF-HFP for 670 continuous charge−discharge cycling at 100 mA cm^{-2}(b) Current rate performance of 45-C−CNC/PVDF-HFP, 45-CNC/PVDF-HFP, and commercial Nafion 115. (c) Charge−discharge profiles of 45-C−CNC/PVDF-HFP at different current densities of 40, 60, 80, 100, 120, and 150 mA cm^{-2}. (d) Comparison of charge−discharge profiles of 45-C−CNC/PVDF-HFP and Nafion 115 at 100 mA cm^{-2}. (e) Coulombic efficiency, (f) voltage efficiency, and (g) energy efficiency of 45-C−CNC/PVDF-HFP, and Nafion 115 at different current densities of 40, 60, 80, 100, 120, and 150 mA cm^{-2}.

CNC/PVDF-HFP, and Nafion 115 membranes. Respectively, they achieved breaking stresses of 28, 34, 58, 61, 44, 65, and 20 MPa, elongations at break of 7.2, 10.1, 5.2, 4.9, 7.5, 4.2, and 155.5%, and Young's moduli of 3.9, 3.4, 11.2, 12.4, 5.9, 15.47, and 0.1%. Young's moduli for all of the CNC/PVDF-HFP membranes are much higher than that of Nafion 115, which indicates a much higher resistance to deformation and better shape stability for all the CNC/PVDF-HFP membranes. It is apparent that with the increasing CNC content, the tensile strength increased, and a reinforcing effect was observed. However, a loss in ductility was accompanied, which can be attributed to the high rigidity and increased crystallinity of the membranes. Additionally, the Nafion membrane has a much lower tensile strength compared to all of the CNC/PVDF-HFP membranes but has a much higher strain (155%) due to its polymeric building unit. The 45-CNC/PVDF-HFP displayed the highest elongation at the break with decent tensile stress, while the 60-CNC/PVDF-HFP membrane displayed the highest breaking stress and Young's modulus. Furthermore, the elongation at the break further decreased, while the tensile strength was increased for the calendared membranes due to the calendaring causing an increase in densification. Therefore, 45-CNC/PVDF-HFP and 60-CNC/PVDF-HFP membranes were chosen for calendaring and battery performance evaluation.

Further, to optimize the calendaring conditions, the calendaring was initially conducted for 45-C−CNC/PVDF-HFP at 60 °C, and the number of calendaring passes in each calendaring direction was varied (Table S2). Electrochemical impedance spectra (EIS) (Figure S6) and mechanical proper-

DOI: 10.1021/acs.nanolett.9b03964
Nano Lett. XXXX, XXX, XXX−XXX

ties (Figure S7) of each sample were also compared to determine the optimized calendaring direction. Based on the mechanical properties, it was first determined that the calendaring direction should only be in the machine direction (the direction at which the calendaring was first conducted). However, the calendaring caused a significant increase in the area resistance, so the calendaring temperature was increased from 60°C to 90°C to reduce this resistance. Next, the number of passes was optimized (Table S3). The results indicate that the optimal number of passes is two for calendaring in the machine direction at 90 °C (Figures S8 and S9), and this condition was used for the rest of the experiments. It is worth noting that the 45-CNC/PVDF-HFP membrane was cycled in the flow cell at 40 mA cm^{-2}, but the capacity faded within the first 25 cycles (Figure S10) due to the generation of visible cracks (Figure S11) and pinholes (Figure S12), which were observed in the SEM images of the membrane after cycling. Hence, the calendaring is a crucial step to enhance the longevity of the membranes.

Furthermore, Figure 4c demonstrates the proton conductivity of the membranes with varying CNC content and Nafion 115. The proton conductivity is extremely crucial as it governs the ohmic potential drop across the membrane and, therefore, impacts the overall performance of the battery. The obtained values for the proton conductivities (calculated using the high frequency resistance of the EIS curves, as shown in Figure S13 and eqs 2 and 3 in Experimental Section) are 0.002, 0.013, 0.014, 0.015, 0.014, 0.016, and 0.015 s cm^{-1} for 40-CNC/PVDF-HFP, 45-CNC/PVDF-HFP, 50-CNC/PVDF-HFP, 60-CNC/PVDF-HFP, 45-C−CNC/PVDF-HFP, 60-C−CNC/PVDF-HFP, and Nafion 115, respectively. The proton conductivities of all membranes except 40-CNC/PVDF-HFP are very similar to Nafion 115. Moreover, the trend indicates a direct correlation between proton conductivity and CNC content, which can be attributed to the highly interconnected hydrophilic nanocluster formation because of the intrinsic ion-exchange ($-SO_3H$ and $-OH$) groups of CNCs. Further improvements in proton conductivities of the membranes can be expected by lowering the pK_a values of CNCs through various surface modifications. Additionally, contact angles of the membranes were measured (Figure S14), which decrease with the increase in CNC content due to the hydrophilicity of CNC. It is worth noting that the effect of calendaring on proton conductivity is negligible. The rate of vanadium ion (VO^{2+}) permeation was measured (Figure 4d) using a diffusion cell (Figure S15), where a reverse trend of CNC content to the VO^{2+} permeation rate was observed. When compared to Nafion, all CNC/PVDF-HFP membranes exhibited significantly lower vanadium permeation, irrespective of being significantly thinner, indicating excellent selectivity of the CNC/PVDF-HFP, which is due to the homogeneous distribution and nanosize of the CNCs. Overall, because of its high proton conductivity along with its excellent VO^{2+} ion inhibition, the 45-C−CNC/PVDF-HFP membrane is expected to achieve impressive battery performance. As expected, the flow cell assembled using the 45-C−CNC/PVDF-HFP membrane displayed excellent electrochemical performance, as demonstrated in Figure 5 and Figure S16.

Moreover, the long-term stability for the membranes implemented in the RFBs is crucial because of the harsh acidic and oxidizing operating conditions. Therefore, to better investigate the chemical stability of the 45-C−CNC/PVDF-HFP, a VRFB assembled using a 45-C−CNC/PVDF-HFP membrane was continuously cycled at a constant current density of 100 mA cm^{-2} and charged at a constant voltage of 1.65 V after every 150 cycles (Figure 5a). The battery with the 45-C−CNC/PVDF-HFP membrane demonstrated an average CE of 97.8% with an excellent capacity retention of 90% of its initial capacity after 150 cycles. The cell regained most of its capacity after every constant voltage charging process without any decay in CE and retained 80% of its initial capacity after 670 cycles. We presume the occurrence of two different phenomena with the galvanostatic cycling that causes the capacity fades with the increase in cycle numbers: (1) even though the crossover of the 45-C−CNC/PVDF-HFP membrane is lower compared to the Nafion 115 membrane, the cell assembled using the 45-C−CNC/PVDF-HFP membrane still shows a gradual decay in capacity during the galvanostatic cycling with the increase in cycle number due to the migration of vanadium ions from one side to the other; (2) during galvanostatic cycling, the system resistance increases, which causes a gradual decrease in energy efficiency with the increase in cycle number. This increase in overpotential moves the charging and discharging curves near the cut off voltage.[30] As a result, the cell cannot completely charge and discharge at the high current density of 100 mA cm^{-2}. A potentiostatic hold at 1.65 V after every 150 cycles rebalance the electrolyte by complete conversion of vanadium to VO_2^+ and V^{2+} in the positive and negative sides of the cell, respectively. As a result of one constant voltage charging at the 150th cycle, the capacity in the following cycles is recovered, and the cell can cycle for more than 600 times in total, which verifies the excellent structural and mechanical stability of the membrane. Therefore, the 45-C−CNC/PVDF-HFP membrane was charged at a constant voltage of 1.65 V after every 150 cycles to fully charge/discharge the electrolyte and rebalance the electrolytes due to crossover. It is worth noting that the preparation of CNC involves hydrolysis of cellulose in strong sulfuric acid, where the disordered and paracrystalline regions of cellulose are preferentially hydrolyzed. However, the crystalline regions remain intact, indicating their higher resistance to acid attack and, therefore, are highly stable in the corrosive, acidic, and oxidizing environment.

The current rate performance of the full cell, as shown in Figure 5b, was achieved by running the cell at six different current densities ranging from 40 mA cm^{-2} to 150 mA cm^{-2} for five consecutive cycles at each current density. The full cell had capacities of 22.99, 21.88, 19.59, 17.81, 16.35, and 14.97 A h L^{-1} at current densities of 40, 60, 80, 100, 120, and 150 mA cm^{-2}, respectively. After these cycles, the battery was returned to the initial current density of 40 mA cm^{-2}, where it regained 96.7% of its original capacity. It indicates outstanding stability attributable to the low vanadium crossover and high chemical stability of the 45-C−CNC/PVDF-HFP membrane. The corresponding charge−discharge profiles of the 45-C−CNC/PVDF-HFP membrane at different current densities (Figure 5c) exhibit an increasing overpotential, causing a gradual reduction in the achieved capacity with the increase in current density. This behavior can be attributed to the increased ohmic loss and mass transport limitations at higher current densities. Figure 5d demonstrates the charge−discharge profiles of the 45-C−CNC/PVDF-HFP membrane compared with the Nafion 115 membrane at the same current density of 100 mA cm^{-2}. The Nafion 115 membrane displays a higher charge−discharge overpotential compared to the 45-C−CNC/PVDF-HFP membrane, which can be attributed to the high

DOI: 10.1021/acs.nanolett.9b03964
Nano Lett. XXXX, XXX, XXX−XXX

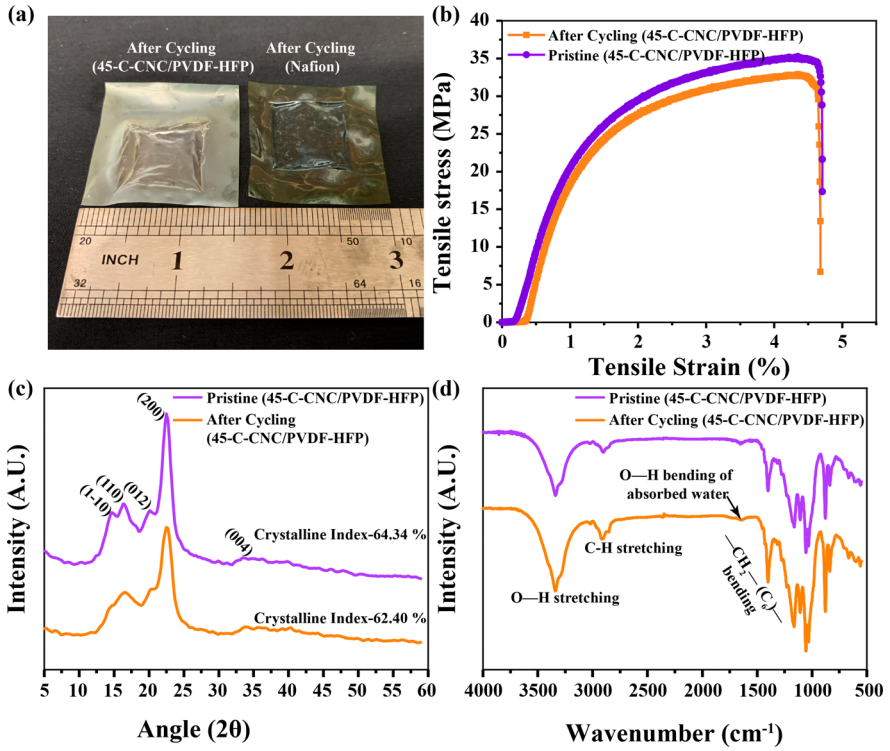

Figure 6. Post-mortem analysis of the 45-C−CNC/PVDF-HFP membrane before and after cycling the VRFB. (a) Digital picture of the 45-C−CNC/PVDF-HFP membrane and Nafion 115 membrane after cycling. (b) Stress vs strain curves, (c) XRD patterns, and (d) FTIR spectra of the 45-C−CNC/PVDF-HFP membrane before and after cycling the VRFB.

proton conductivity and lower thickness of the 45-C−CNC/PVDF-HFP membrane, leading to a lower voltage drop than that of the Nafion 115. Remarkably, the 45-C−CNC/PVDF-HFP membrane demonstrated a high CE of 94.5, 96.3, 97.4, 98.2, 98.6, and 99.6% (Figure 5e) at the current densities of 40, 60, 80, and 100, 120, and 150 mA cm^{-2}, respectively, whereas the Nafion 115 membrane achieves CEs of 92.5, 94.4, 95.3, 96.3, 96.7, and 97.3% at the same current densities of 40, 60, 80, and 100, 120, and 150 mA cm^{-2}, respectively. The improved Coulombic efficiencies of the 45-C−CNC/PVDF-HFP membrane indicate a lower capacity loss and are attributable to the excellent ion selectivity, leading to negligible vanadium crossover. It is worth mentioning that the CE increases with the increase in the current density due to the shorter charge−discharge time at high current densities.[31] However, a reverse trend of a decline in voltage efficiencies with an increase in current density was observed for both the membranes because of the higher ohmic polarization and overpotential at higher current densities.[32] Consequently, the obtained VE (Figure 5f) at similar operating cell conditions for 45-C−CNC/PVDF-HFP are 94.3, 92.6, 91.1, 89.9, 86.6, and 85.6% and for Nafion 115 are 94.2, 89.2, 86.2, 83.2, 80.3, and 78.2% at the current densities of 40, 60, 80, 100, 120, and 150 mA cm^{-2}, respectively. Meanwhile, the 45-C−CNC/PVDF-HFP membrane demonstrates EEs of 89.1, 89.2, 88.7, 88.2, 85.3, and 85.2% at current densities of 40, 60, 80, 100, 120, and 150 mA cm^{-2}, while the EEs for Nafion 115 are 87.2, 84.2, 82.1, 80.2, 77.7, and 76.1%, respectively, at the same current densities (Figure 5g). These excellent VEs and EEs of the 45-C−CNC/PVDF-HFP membrane are due to the lower area-specific resistance of the membrane. Note that, even though the proton conductivity of the Nafion 115 membrane is slightly higher compared to the 45-C−CNC/PVDF-HFP membrane, the ASR of the 45-C−CNC/PVDF-HFP is lower compared to the Nafion 115 since the thickness of the 45-C−CNC/PVDF-HFP membrane is ∼50 μm less. Additionally, the current rate performance of the 60-C−CNC/PVDF-HFP membrane, for which the SEM images are shown in Figures S17 and S18, was evaluated (Figure S19), as the proton conductivity of the membrane is higher than Nafion 115. However, the membrane displayed a CE of ∼96% at 100 mA cm^{-2} and, due to the poor structural stability, a gradual capacity fade at each cycle and higher vanadium crossover compared to the 45-C−CNC/PVDF-HFP membrane (Figure S20).

Furthermore, to confirm the chemical stability of the 45-C−CNC/PVDF-HFP membrane, post-mortem analysis of the membrane was conducted after using the membrane for more than 2 weeks (120 cycles). The 45-C−CNC/PVDF membrane retains its structural integrity and robustness (Figure 6a) without any noticeable changes after exposure to the harsh oxidizing environment for more than 2 weeks, which verifies its excellent physical stability. The wrinkles observed at the center part of the membrane occurred due to the dehydration of the membrane and disappeared after soaking the membrane in water. Further, the stress−strain curves for the 45-CNC/PVDF-HFP membrane before and after cycling (Figure 6b) exhibit breaking stresses of 34.68 and 32.52 MPa and elongations at breaks of 4.67 and 4.63%, respectively. It is evident that the breaking stress and the elongations at the break of the 45-CNC/PVDF-HFP membrane are similar before and after cycling, most likely due to the high chemical and mechanical stability of the membrane. Additionally, X-ray diffraction patterns (XRD) of the 45-C−CNC/PVDF-HFP membrane before and after cycling demonstrate that the membranes retain the characteristic diffraction peaks of CNCs even after long-term cycling. CNCs in the 45-C−CNC/PVDF-

DOI: 10.1021/acs.nanolett.9b03964
Nano Lett. XXXX, XXX, XXX−XXX

HFP membranes before and after cycling display peaks at similar 2θ angles of ~14.8, 16.3, 20.4, 22.7, and 34.5 corresponding to the reflection planes 1−10, 110, 012, 200, and 004, respectively (Figure 6c).[33] Moreover, the crystalline index (CrI) of the CNCs in the 45-C−CNC/PVDF-HFP membrane before and after cycling was also calculated using the Segal equation (see Experimental Section).[34−36] The CrI for CNCs was found to be about 64.34 and 62.40% in the 45-C−CNC/PVDF-HFP membrane before and after cycling. Therefore, the XRD patterns and CrI consistency for the 45-C−CNC/PVDF-HFP membrane after cycling indicates that the CNC can maintain its inherent crystalline structure after cycling of the membrane for a long time.

Likewise, the absence of any changes in the Fourier transform infrared (FTIR) spectra of the 45-C−CNC/PVDF-HFP membrane before and after cycling (Figure 6d) confirms the outstanding chemical stability of the membrane. The 45-C−CNC/PVDF-HFP membrane before and after cycling featured distinct hydroxyl group peaks located at 3340 cm^{-1}, which corresponds to the O−H stretching of the three hydroxyl groups of cellulose.[37] It is also interesting to note that the peaks at 2900 and 1410 cm^{-1} appeared in both the curves before and after cycling, corresponding to the C−H stretching vibration and $-CH_2-(C_6)-$ bending vibrations,[38] respectively. There is a small peak present at 1640 cm^{-1}, which corresponds to the intramolecular hydrogen bonding that arises due to the cellulose−water interaction, leading to −OH bending of absorbed water.[39] Therefore, the XRD and FTIR results confirm that the 45-C−CNC/PVDF-HFP membrane possesses strikingly high chemical stability in the harsh environment of VRFB.[13]

In conclusion, a homogeneous and highly stable proton conductive membrane was designed with high selectivity consisting of nanorod CNCs enmeshed in a PVDF-HFP matrix. Inspiringly, the intrinsic pendant −OH groups, highly acidic $-SO_3H$ groups, and enormous hydrogen bonding of CNCs construct highly interconnected hydrophilic ionic nanoclusters that impart superior proton conductivity of 0.014 s cm^{-1} to the 45-C−CNC/PVDF-HFP membrane. In addition, high crystallinity of CNCs ensures exceptionally high chemical stability in the harsh operating condition (3 M H_2SO_4) of aqueous inorganic RFB, which solves the chemical stability issues of existing nonperfluorinated ion-exchange membranes. The CNCs provided superior proton conductivity, while the PVDF-HFP serves as the hydrophobic matrix and provides ionic selectivity and mechanical flexibility to the membrane. As a result, the VRFB assembled with the 45-C−CNC/PVDF-HFP membrane exhibited CE of ~98.2%, EE of ~88.2%, and a stable cycling performance for more than 650 cycles at a current density of 100 mA cm^{-2}. The results indicate that the idea of incorporating hydrophilic, durable, and abundant CNCs with hydrophobic PVDF-HFP to obtain high performance and the stable membrane is promising for aqueous flow batteries and could be an alternative to expensive Nafion membranes. The abundant and low-cost CNC/PVDF-HFP membrane provides a promising strategy toward the design and fabrication of highly stable proton exchange membranes for large-scale industrialization.

Experimental Section. *CNC Synthesis.* The preparation of CNCs by acid-catalyzed hydrolysis was described in detail in our previously published work.[40] The hydrolysis of microcrystalline cellulose (Sigma-Aldrich, USA) was conducted by adding 50 g of microcrystalline cellulose to 500 mL of 64.0 wt % sulfuric acid (Sigma-Aldrich, USA) while stirring the mixture continuously. The temperature was maintained at 50 °C for 1 h, and the reaction was stopped by quenching the solution with 5 L of water. The obtained mixture was kept at room temperature to allow the CNCs to settle down, and the excess water was carefully removed from the solution. The suspension was then washed with deionized water by repeated centrifuging, where the supernatant was collected and dialyzed in deionized water for at least 7 days using regenerated cellulose dialysis membranes with a molecular weight cutoff of 12 000−14 000 Da.

Membrane Preparation. The obtained CNC in deionized water was first sonicated for 2 h and then freeze-dried for ~48 h to acquire dried CNC flakes. To prepare the CNC/PVDF composite membrane, the freeze-dried CNC flakes were first dispersed in dimethylformamide (DMF, Sigma-Aldrich, USA) by mixing vigorously for 1 h. They were then added to the 10 wt % PVDF-HFP (Sigma-Aldrich, USA) in DMF solution according to the desired weight ratio of CNC and PVDF-HFP. The mixture was probe sonicated (400 W, 20 kHz, Sonic) for 1 h in an ice bath at 20% amplitude with a consecutive 1 s pulse and 1 s rest. Then the mixture was degassed in a vacuum desiccator to remove the bubbles. Finally, the viscosity of the solution was adjusted by adding an additional DMF to obtain the desired consistency for casting. The as-prepared solution was cast using a Compact Tape Casting Coater (Model-MSK-AE A-I, MTI Corporation, USA) on a glass substrate.

Further, the casted membrane was dried at 60 °C for 48 h in an oven to remove the solvent and then calendared (Hobsen Corporation HSTK-1515H, USA) at 90 °C to get the final membrane. The membranes were then treated by boiling in deionized water at 85 °C for 15 min, followed by soaking in 5% hydrogen peroxide (Fisher Scientific, USA) for 30 min and finally immersed for 30 min in a 0.1 M sulfuric acid solution for ion exchange. The membrane was washed thoroughly with deionized water after each step. The treated membranes were then stored in deionized water at room temperature.

Characterizations. The intensity of particle distributions for the redispersed CNC in water and DMF were measured using dynamic light scattering (DLS) (Zetasizer Nano ZS, Malvern Instruments, USA), which has a 173° detector and 50 mW 633 nm laser source. Freeze-dried CNC was redispersed in water (1 wt %) and DMF (1 wt %) and probe sonicated (400 W, 20 kHz, Sonic) for 15 min in an ice bath at 20% amplitude with a consecutive 1 s pulse and 1 s rest to prepare the stock solution. Further, the stock solution was diluted 10-fold to obtain the DLS measurements. Before starting the measurements, the temperature was equilibrated to 25 °C for 180 s, and a refractive index of 1.48 was used for CNC for all measurements.[41] The viscosity of dispersants was calculated by the equipment to be 1.33 for water and 1.431 for DMF. The obtained data were analyzed by Malvern nanosizer software using the normal resolution cumulants analysis method to obtain the intensity of the particle distribution.

The morphology of the membranes was investigated by a Zeiss Supra 25 SEM using 5 keV accelerating voltage. The cross sections of the membranes were prepared by cutting the membranes in liquid nitrogen and sputter coating before imaging. TEM images of CNC were taken using a JEM-1010 transmission electron microscope (JEOL, Japan) at an accelerating voltage of 80 kV. The sample was prepared by dropping a diluted CNC solution on a 300 mesh copper grid

DOI: 10.1021/acs.nanolett.9b03964
Nano Lett. XXXX, XXX, XXX−XXX

coated with carbon film and then negatively staining with 1.5 wt % phosphotungstic acid.

Further, the morphology of CNC was also investigated using an AFM (Parks Scientific XE7, Canada) in the noncontact imaging mode. To prepare the sample, 10 μL of 0.001 wt % CNC suspension was deposited onto a silica surface and air-dried. The X-ray diffraction (XRD) patterns of the samples were recorded for 2θ ranging from 5° to 60° on PANalytical/Philips X'Pert Pro with Cu Kα radiation. The crystalline index (CrI) was calculated by the Segal method,[36] as shown in eq 1.

$$\mathrm{CrI} = \left[\frac{I_{200} - I_{\mathrm{am}}}{I_{200}}\right] \times 100 \tag{1}$$

Where CrI represents the relative degree of crystallinity, I_{002} indicates the intensity of the 002 lattice diffraction at a 2θ value of 22.7° (represents both the crystalline and amorphous region), and I_{am} represents the intensity of diffraction at 2θ = 18° (represents only the amorphous region).

The FTIR spectra of the membranes were recorded using a Nicolet FTIR 5700 spectrophotometer (Bruker, Germany) in transmission mode over the range of 500 to 4000 cm^{-1} with a 4 cm^{-1} resolution at 25 °C. The mechanical properties of the membranes were tested using an Instron testing system at 25 °C at a constant crosshead speed of 5 mm/min with samples of approximately 5 mm × 15 mm.

Area Resistance Measurement and Proton Conductivity Calculation. The area resistance of the prepared membranes was measured from a static flow cell assembled using a graphite felt electrode with an effective area of 5 cm^2. A solution of 1 M $VOSO_4$ in 3 M H_2SO_4 was injected into the cell before each test. Electrochemical impedance spectroscopy using a Biologic SP 150 (USA) potentiostat was conducted by applying a sinusoidal voltage waveform of amplitude 10 mV added to an offset voltage with and without a membrane, and corresponding resistances can be denoted as R_{S1} and R_{S2} (the high frequency intercepts with the real (x) axis). EIS spectra of the VRFB full cell contains a semicircle at the low-frequency region (R_{ct}) corresponding to the faradic charge transfer at the electrode−electrolyte interfaces, while the high-frequency intercept with the horizontal axis (X) indicates the ohmic resistance of the cell (R_s). The R_{ct} is in parallel with the electrode−electrolyte double-layer capacitance (Figure S21). However, the constant phase element (CPE_1) was used instead of capacitance due to the uneven potential distribution in the porous graphite electrode, which addresses the nonideal behavior of the electrode−electrolyte double-layer capacitance, where the CPE_2 corresponds to the mass transfer capacitance. The Zsimpwin software was used for the fitting of the EIS curves using the equivalent circuit shown in Figure S21 in order to obtain the R_{S1} and R_{S2} values. The frequency of the sinusoidal voltage was varied stepwise from 1 MHz to 100 mHz, with 6 points per decade in logarithmic spacing. The area resistance R was calculated by the following equation:

$$R = (R_{S1} - R_{S2}) \times A \tag{2}$$

where A is the active area of the membrane.

The proton conductivity was calculated by the following equation:

$$\sigma = \frac{L}{R} = \frac{L}{(R_{S1} - R_{S2}) \times A} \tag{3}$$

where σ is the proton conductivity (s cm^{-1}) of the membranes, L is the membrane thickness (cm), and R is the area resistance (Ω).

Vanadium Permeability. The permeability of VO_2^+ was found experimentally to characterize the ion selectivity of the membranes. A diffusion cell, where the two chambers are separated by a membrane, was used to evaluate the permeability of vanadium ions through the membrane being tested. One chamber was filled with 10 mL of 1 M $VOSO_4$ in a 3 M H_2SO_4 aqueous solution, and the other chamber was filled with 10 mL of 3 M H_2SO_4 aqueous solution. A sample of 500 μL of solution from the H_2SO_4-filled chamber was collected at a regular time interval, and the same volume of fresh solution was then added to the same chamber to maintain an equal volume on both sides. The absorbance of each sample at 760 nm wavelength was detected using a UV−vis spectrometer (Agilent 8453, USA). A calibration curve of $VOSO_4$ was obtained at 760 nm wavelength, and the vanadium concentration corresponding to each measured absorbance was calculated using the calibration curve.

Flow Cell Test. The setup of the flow cell is described in detail in our previously published work.[42−44] The active area of the electrodes for both sides is 5 cm^2. The SGL graphite felt electrodes were treated at 400 °C for 30 h in the air. The electrolytes were pumped at a flow rate of 40 mL min^{-1} using a peristaltic pump (Masterflex L/S Economy Drive, USA), and the flow rate was kept constant for all of the experiments. The negative side was sparged with nitrogen gas before running and appropriately sealed to prevent oxygen exposure. Initially, the electrolytes were prepared by dissolving 1 M $VOSO_4$ (Sigma-Aldrich, USA, 99%) in 3 M H_2SO_4 (Sigma-Aldrich, USA, 97%) solution. To prepare the positive and negative side electrolytes, the cell was charged at a constant voltage of 1.65 V until the current drops below 5 mA, which indicated complete conversion to V(V) and V(II) on the positive and negative sides, respectively. The electrochemical charge−discharge of the flow cell was conducted using a potentiostat (LAND, China) under a constant current density ranging from 40 to 150 mA cm^{-2}.

■ ASSOCIATED CONTENT

Supporting Information

The Supporting Information is available free of charge on the ACS Publications website at DOI: 10.1021/acs.nanolett.9b03964.

Cost analysis of the 45-C−CNC/PVDF-HFP membrane, characterizations of CNC, assessment of redispersibility of freeze-dried CNC, optimization of calendering conditions for 45-C−CNC/PVDF-HFP membrane, optimization of the ratio of CNC and PVDF-HFP in the CNC/PVDF-HFP membrane, and characterizations and cell performance of the 60-C−CNC/PVDF-HFP membrane (PDF)

■ AUTHOR INFORMATION

Corresponding Authors

*E-mail: wei.wang2@rogerscorporation.com.
*E-mail: h.zhu@neu.edu.

ORCID

Alolika Mukhopadhyay: 0000-0003-2085-7063
Hongli Zhu: 0000-0003-1733-4333

DOI: 10.1021/acs.nanolett.9b03964
Nano Lett. XXXX, XXX, XXX−XXX

Notes

The authors declare no competing financial interest.

■ ACKNOWLEDGMENTS

Rogers Corporation financially supported this research by awarding a grant to H.Z. We acknowledge the Kostas Nanomanufacturing Research Center for sharing the scanning electron microscope, atomic force microscope, and X-ray diffraction measurement devices. We would also like to extend our gratitude to Northeastern University Center for Renewable Energy Technology (NUCRET) facilities for allowing us to use Fourier transform infrared spectroscopy. Additionally, we would like to thank Dr. Carol Livermore for sharing the Instron machine to measure the mechanical properties of the membranes.

■ REFERENCES

(1) Li, X.; Zhang, H.; Mai, Z.; Zhang, H.; Vankelecom, I. *Energy Environ. Sci.* **2011**, *4*, 1147−1160.
(2) Noack, J.; Wietschel, L.; Roznyatovskaya, N.; Pinkwart, K.; Tübke, J. *Energies* **2016**, *9*, 627.
(3) Yuan, Z.; Zhang, H.; Li, X. *Chem. Commun.* **2018**, *547570*−7588.
(4) grosse Austing, J.; Kirchner, C. N.; Komsiyska, L.; Wittstock, G. *J. Membr. Sci.* **2016**, *510*, 259−269.
(5) Trogadas, P.; Pinot, E.; Fuller, T. F. *Electrochem. Solid-State Lett.* **2012**, *15*, A5−A8.
(6) Wang, N.; Peng, S.; Lu, D.; Liu, S.; Liu, Y.; Huang, K. *J. Solid State Electrochem.* **2012**, *16*, 1577−1584.
(7) Lin, C.-H.; Yang, M.-C.; Wei, H.-J. *J. Power Sources* **2015**, *282*, 562−571.
(8) Yang, R.; Cao, Z.; Yang, S.; Michos, I.; Xu, Z.; Dong, J. *J. Membr. Sci.* **2015**, *484*, 1−9.
(9) Xi, J.; Wu, Z.; Teng, X.; Zhao, Y.; Chen, L.; Qiu, X. *J. Mater. Chem.* **2008**, *18*, 1232−1238.
(10) Schwenzer, B.; Kim, S.; Vijayakumar, M.; Yang, Z.; Liu, J. *J. Membr. Sci.* **2011**, *372*, 11−19.
(11) Zeng, J.; Jiang, C.; Wang, Y.; Chen, J.; Zhu, S.; Zhao, B.; Wang, R. *Electrochem. Commun.* **2008**, *10*, 372−375.
(12) Luo, Q.; Zhang, H.; Chen, J.; You, D.; Sun, C.; Zhang, Y. *J. Membr. Sci.* **2008**, *325*, 553−558.
(13) Yuan, Z.; Li, X.; Hu, J.; Xu, W.; Cao, J.; Zhang, H. *Phys. Chem. Chem. Phys.* **2014**, *16*, 19841−19847.
(14) Habibi, Y.; Lucia, L. A.; Rojas, O. J. *Chem. Rev.* **2010**, *110*, 3479−3500.
(15) Trache, D.; Hussin, M. H.; Haafiz, M. M.; Thakur, V. K. *Nanoscale* **2017**, *9*, 1763−1786.
(16) de Assis, C. A.; Houtman, C.; Phillips, R.; Bilek, E.; Rojas, O. J.; Pal, L.; Peresin, M. S.; Jameel, H.; Gonzalez, R. *Biofuels, Bioprod. Biorefin.* **2017**, *11*, 682−700.
(17) *Market Research Store*. http://www.marketresearchstore.com/news/.
(18) Pei, A.; Malho, J.-M.; Ruokolainen, J.; Zhou, Q.; Berglund, L. A. *Macromolecules* **2011**, *44*, 4422−4427.
(19) Moon, R. J.; Martini, A.; Nairn, J.; Simonsen, J.; Youngblood, J. *Chem. Soc. Rev.* **2011**, *40*, 3941−3994.
(20) Wu, Q.; Mei, C.; Zhang, X.; Lei, T.; Zhang, Z.; Li, M., Electrospun Poly (Ethylene Oxide) Fibers Reinforced with Poly (Vinylpyrrolidone) Polymer and Cellulose Nanocrystals. In *Electrospinning Method Used to Create Functional Nanocomposites Films*; IntechOpen, 2018.
(21) Moon, R.; Beck, S.; Rudie, A. *Review Process: Non-Refereed (Other)*; 2013.
(22) Batista, M. D. R.; Drzal, L. T. *Compos. Sci. Technol.* **2018**, *164*, 274−281.
(23) Deng, T.; Wang, Y.; Dufresne, A.; Lin, N. *Carbohydr. Polym.* **2018**, *181*, 111−118.
(24) Shin, D. W.; Guiver, M. D.; Lee, Y. M. *Chem. Rev.* **2017**, *117*, 4759−4805.
(25) Sahlin, K.; Forsgren, L.; Moberg, T.; Bernin, D.; Rigdahl, M.; Westman, G. *Cellulose* **2018**, *25*, 331−345.
(26) Kreuer, K.-D.; Paddison, S. J.; Spohr, E.; Schuster, M. *Chem. Rev.* **2004**, *104*, 4637−4678.
(27) Pourcelly, G.; Oikonomou, A.; Gavach, C.; Hurwitz, H. *J. Electroanal. Chem. Interfacial Electrochem.* **1990**, *287*, 43−59.
(28) Beck, S.; Bouchard, J.; Berry, R. *Biomacromolecules* **2012**, *13*, 1486−1494.
(29) Peng, Y.; Gardner, D. J.; Han, Y.; Kiziltas, A.; Cai, Z.; Tshabalala, M. A. *Cellulose* **2013**, *20*, 2379−2392.
(30) Lin, K.; Gómez-Bombarelli, R.; Beh, E. S.; Tong, L.; Chen, Q.; Valle, A.; Aspuru-Guzik, A.; Aziz, M. J.; Gordon, R. G. *Nature Energy* **2016**, *1*, 16102.
(31) Zhang, H.; Zhang, H.; Zhang, F.; Li, X.; Li, Y.; Vankelecom, I. *Energy Environ. Sci.* **2013**, *6*, 776−781.
(32) Xu, W.; Zhao, Y.; Yuan, Z.; Li, X.; Zhang, H.; Vankelecom, I. F. J. *Adv. Funct. Mater.* **2015**, *25*, 2583−2589.
(33) Lin, N.; Dufresne, A. *Nanoscale* **2014**, *6*, 5384−5393.
(34) El Miri, N.; Abdelouahdi, K.; Barakat, A.; Zahouily, M.; Fihri, A.; Solhy, A.; El Achaby, M. *Carbohydr. Polym.* **2015**, *129*, 156−167.
(35) Neto, W. P. F.; Silvério, H. A.; Dantas, N. O.; Pasquini, D. *Ind. Crops Prod.* **2013**, *42*, 480−488.
(36) Segal, L.; Creely, J.; Martin, A., Jr; Conrad, C. *Text. Res. J.* **1959**, *29*, 786−794.
(37) Johar, N.; Ahmad, I.; Dufresne, A. *Ind. Crops Prod.* **2012**, *37*, 93−99.
(38) Man, Z.; Muhammad, N.; Sarwono, A.; Bustam, M. A.; Kumar, M. V.; Rafiq, S. *J. Polym. Environ.* **2011**, *19*, 726−731.
(39) Abraham, E.; Kam, D.; Nevo, Y.; Slattegard, R.; Rivkin, A.; Lapidot, S.; Shoseyov, O. *ACS Appl. Mater. Interfaces* **2016**, *8*, 28086−28095.
(40) Cheng, Z.; Ye, H.; Cheng, F.; Li, H.; Ma, Y.; Zhang, Q.; Natan, A.; Mukhopadhyay, A.; Jiao, Y.; Li, Y.; Liu, Y.; Zhu, H. *Adv. Mater. Interfaces* **2019**, *0*, 1802010.
(41) Leng, T. *Cellulose Nanocrystals: Particle Size Distribution and Dispersion in Polymer Composites*; Université d'Ottawa/University of Ottawa, 2016.
(42) Mukhopadhyay, A.; Zhao, H.; Li, B.; Hamel, J.; Yang, Y.; Cao, D.; Natan, A.; Zhu, H. *ACS Applied Energy Materials* **2019**, *2*, 7425−7437.
(43) Mukhopadhyay, A.; Yang, Y.; Li, Y.; Chen, Y.; Li, H.; Natan, A.; Liu, Y.; Cao, D.; Zhu, H. *Adv. Funct. Mater.* **2019**, *29*, 1903192.
(44) Mukhopadhyay, A.; Hamel, J.; Katahira, R.; Zhu, H. *ACS Sustainable Chem. Eng.* **2018**, *6*, 5394−5400.

DOI: 10.1021/acs.nanolett.9b03964
Nano Lett. XXXX, XXX, XXX−XXX